Exploring equilibrium conditions in liquid metal dealloying of powders by in situ synchrotron X-ray diffraction

Louis Lesage, Christophe Le Bourlot, Eric Maire, Takeshi Wada, Hidemi Kato, Wolfgang Ludwig, Nicolas Mary, Pierre-Antoine Geslin

MTLA 36 (2024) 102177

Contents lists available at ScienceDirect

Materialia

journal homepage: www.elsevier.com/locate/mtla

Full length article

Exploring equilibrium conditions in liquid metal dealloying of powders by in situ synchrotron X-ray diffraction

Louis Lesage [a,b,c,*], Christophe Le Bourlot [a], Eric Maire [a], Takeshi Wada [d], Hidemi Kato [c,d], Wolfgang Ludwig [a,e], Nicolas Mary [a,c], Pierre-Antoine Geslin [a,**]

[a] CNRS, INSA Lyon, Universite Claude Bernard Lyon 1, MATEIS, UMR 5510, Villeurbanne Cedex, 69621, France
[b] Department of Materials Science, Graduate School of Engineering, Tohoku University, Sendai, 980-8579, Japan
[c] ELyTMaX IRL3757, CNRS, Univ Lyon, INSA Lyon, Centrale Lyon, Universite Claude Bernard Lyon 1, Tohoku University, Sendai, 980-8577, Japan
[d] Institute for Materials Research, Tohoku University, Sendai, 980-8577, Japan
[e] ESRF - The European Synchrotron, Grenoble, 38043, France

ARTICLE INFO

Keywords:
Dealloying
In situ X-ray diffraction
Synchrotron
Rietveld analysis
Thermodynamic equilibria

ABSTRACT

Liquid metal dealloying is a recently developed method to elaborate micro and nano-porous materials. It consists of the selective dissolution of an alloying element from a precursor alloy by immersing it in a liquid metal bath. In this paper, we monitor the dealloying reaction of Invar ($Fe_{65}Ni_{35}$) powders in liquid Mg using in situ synchrotron X-ray diffraction. Rietveld refinement of the diffraction spectra enables quantifying the evolution of different crystalline phases throughout the process, thereby gaining new insights into the kinetics, phase equilibria, and the role of intermetallics on the reaction. These results are systematically compared to post mortem observations of dealloyed samples, showing a good agreement between both techniques. In particular, we show that adjusting the thermodynamic conditions of the reaction (temperature, FeNi/Mg ratio) enables to tailor the microstructure of the dealloyed powders, by modifying the dealloyed fraction to achieve core–shell structures, and altering the composition of ligaments.

1. Introduction

Liquid metal dealloying (LMD) is an innovative technique to elaborate metals with an open connected porosity. With their high specific surface area, porous materials elaborated with LMD are considered good candidates for catalysis [1,2] and energy storage applications [3,4] and have been attracting increasing attention in the past decade [5–7]. The LMD process consists of immersing a precursor A–B alloy into a liquid metal C. A and B being respectively immiscible and miscible with C, B selectively dissolves into the metallic bath C, while A reorganises into an interconnected structure. After etching in an appropriate acidic solution, the newly formed C–B phase can be selectively removed, leaving behind the desired A porous structure. In contrast with other types of dealloying methods (electrochemical [8,9], vacuum [10], and molten salt dealloying [11]...), LMD holds the advantage of being applicable to a wide range of systems where the target elements are immiscible in Mg [5,12], Ag [13], Bi [14,15] or Cu [16,17].

Among these different LMD systems, some of them such as NiCuAg [18] or TaTiCu [19] display simple thermodynamics features at the dealloying temperature, involving liquid/solid equilibria and large miscibility of the sacrificial element in the bath. In particular, dealloying of TaTi alloys in Cu has been the focus of experimental and numerical studies [16,17,19,20], improving our understanding of the dealloying processes. Such progress opens the possibility to tune the dealloying parameters (dealloying time and temperature, composition of the precursor and the liquid bath) in order to control the features of the porous materials resulting from the dealloying reaction (dealloyed thickness, porosity, ligaments size and composition, ...). In particular, changing the composition of the liquid bath appears as a good leverage to modify the composition of the resulting porous materials [14] as well as its topological connectivity [21]. Recently, LMD was also applied to powders [20,22]: mixing TaTi powders with Cu powders and heating the mix above the melting temperature of Cu leads to the formation of porous Ta particles. It was shown that the ratio between powders in the mix could be modified to control the dealloying fraction and produce partially dealloyed particles with a distinctive core–shell structure, featuring a dense core surrounded by a porous layer.

Nevertheless, most LMD systems display more complicated phase diagrams, increasing the difficulty of controlling the dealloyed materials microstructure. In particular, liquid Mg is often used to dealloy Ni and

* Corresponding author at: CNRS, INSA Lyon, Universite Claude Bernard Lyon 1, MATEIS, UMR 5510, Villeurbanne Cedex, 69621, France.
** Corresponding author.
E-mail addresses: louis.lesage@insa-lyon.fr (L. Lesage), pierre-antoine.geslin@insa-lyon.fr (P.-A. Geslin).

https://doi.org/10.1016/j.mtla.2024.102177
Received 28 June 2024; Accepted 6 July 2024
Available online 9 July 2024

Cu out of metallic alloys in order to form a variety of porous metals and alloys [12,14,23,24]; but Mg forms intermetallic phases with both Ni and Cu and the influence of these compounds on the dealloying reaction remains unclear. In addition, post mortem observations of the dealloyed samples do not enable to gain information on the thermodynamic equilibria taking place during the reaction and do not allow to discriminate the influence of the heating ramp, temperature plateau, and cooling step on the formation of these intermetallic phases and on the resulting microstructure.

Therefore, it seems desirable to monitor the dealloying reaction in situ, as such techniques has been shown to greatly clarify how processes unfold [11,25–27]. In the case of liquid metal dealloying, it would enable to quantify the amount of each phase during the dealloying reaction in order to assess the thermodynamic equilibria taking place during the dealloying reaction and to clarify the role of intermetallic compounds on the dealloying reaction. FeNi dealloyed in Mg appears as an appealing system for such study: upon the dealloying of Ni from the precursor alloy, austenitic FeNi alloys transform into a ferritic structure, enabling to follow the reaction in situ with X-ray diffraction (XRD) as done in Ref. [25].

In this article, we use synchrotron radiation to monitor in situ the dealloying reaction of Invar ($Fe_{65}Ni_{35}$) powders mixed with Mg particles. The use of a powder mix allows us to control carefully the size of the bath (Mg) compared to the amount of precursor as in Ref. [20], thereby exploring different phase equilibria. In contrast with previous works [25], the experimental setup allows for a precise control of the temperature, enabling to discuss the formation of phases in light of equilibrium thermodynamics. Combining in situ XRD with post mortem observations, we discuss how the size of the bath and the temperature influence the resulting microstructure and can be chosen to elaborate core–shell powders.

The paper is organised as follows: in Section 2, we introduce the materials and methods used for the elaboration and the in situ and post mortem characterisation of the dealloyed powders. Section 3 is devoted to the results of in situ monitoring of dealloying by XRD that were compared with post mortem analysis of dealloyed powders. These experiments were conducted at two different target temperatures: 675 °C (Section 3.1) and 750 °C (Section 3.2). In Section 4, we discuss the possibilities and limitations of controlling the features of dealloyed powders through thermodynamics, as well as the role of intermetallic phases in the dealloying reaction.

2. Materials and methods

2.1. System under study

In this work, we choose to focus on the FeNiMg system where FeNi precursors are dealloyed in an Mg liquid bath. The three binary phase diagrams of the system are displayed in Fig. 1. All the phase diagrams in this study were computed with the software Thermo-Calc [28]. The Invar ($Fe_{65}Ni_{35}$) precursor used in this work exhibits an austenitic FCC structure. As shown in Fig. 1.b and Fig. 1.c, Fe and Ni are respectively immiscible and miscible in liquid Mg, which will promote the LMD reaction by allowing the selective dissolution of Ni in the liquid bath. We also note that the Mg–Ni phase-diagram displays the formation of two intermetallic phases (Mg_2Ni and $MgNi_2$) and shows a eutectic transformation L → Mg(hcp) + Mg_2Ni.

Heating Mg above its fusion temperature ($T_m^{(Mg)}$ = 650 °C) triggers the dissolution of Ni in the liquid Mg and thereby enables the dealloying reaction. The FeNiMg system has been the topic of several studies on this dealloying reaction [30], usually including Cr in the precursor alloy [25,30–32] to allow etching and the elaboration of porous materials. Owing to their comparable atomic sizes and chemistry, it is commonly assumed that Cr behaves similarly to Fe as long as it is added in small proportions to avoid the formation of the intermetallic σ phase. These previous works show that the immersion of austenitic Fe(Cr)Ni alloys in liquid Mg leads to the dissolution of Ni in the liquid bath and the formation of Fe(Cr) ligaments with a BCC structure. The FCC → BCC phase transition occurring during the dealloying reaction makes it possible to monitor in situ the reaction thanks to X-ray diffraction [25].

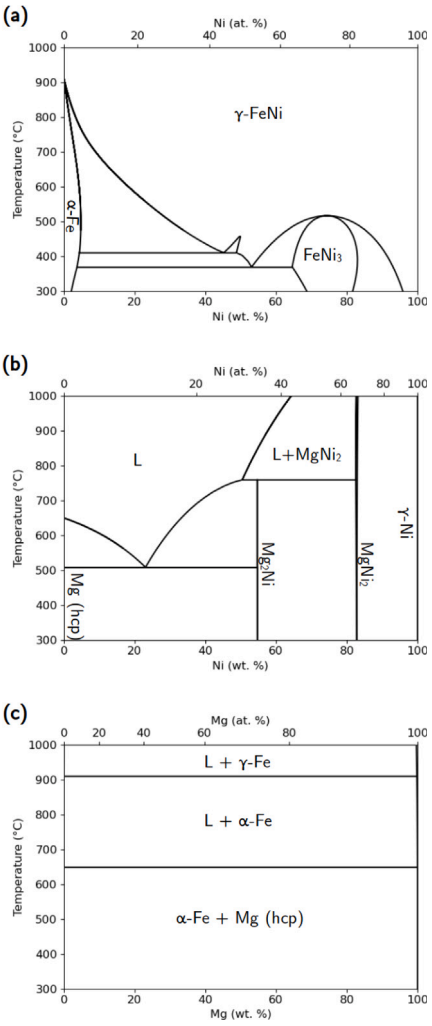

Fig. 1. Binary phase diagrams: (a) Fe–Ni [29]. (b) Mg–Ni [23]. (c) Fe–Mg [23].

The FeNiMg ternary system also holds the advantage of having been thoroughly assessed thermodynamically in Ref. [23]. This database is used to compute the phase diagrams shown in the following section.

2.2. In situ XRD experiment

The in situ X-ray diffraction experiments were performed at the European Synchrotron Radiation Facility, using the beamline ID11. A resistive furnace provided on the beamline allowed us to heat up the sample while following the evolution of diffraction patterns.

2.2.1. Samples preparation

The samples undergoing in situ dealloying experiments were prepared according to the following protocol. As-atomised austenitic Invar powders ($Fe_{65}Ni_{35}$, d_{90v} = 15 µm, GoodFellow, UK) were mixed manually with pure as-atomised Mg powders (purity> 99.8 wt.%, d_{90v} = 15 µm, SFM SA, Switzerland) in various ratios. In the following, the samples will be referred as "InvarMgxx_yyy", xx indicating the wt.% of Mg in the initial mix and yyy the target temperature of the experiment (e.g. the sample "InvarMg10_675" is made from a powder mixture

containing 10 wt% of Mg and 90 wt% of Invar and was dealloyed at 675 °C).

These powders mixtures were inserted in quartz tubes (inner diameter: 1 or 1.5 mm; outer diameter: 3 mm) with a syringe and filled around 1 cm of the tube length. Powders were kept at the top of the tube by an alumina rod maintained by Kanthal wire. After achieving a vacuum of 0.1 Pa the powders were encapsulated in an Ar atmosphere under a pressure of 0.9 bar to prevent oxidation of Mg. Before starting the XRD experiment, the homogeneity of the powder mixture was checked from a X-ray tomography scan performed on the beamline.

2.2.2. Synchrotron experimental setup

A resistive oven was placed around the sample as shown in Fig. 2.a. The temperature of the oven was monitored by a thermocouple placed inside the oven and calibrated from the fusion of Mg powders that have a known melting temperature of 650 °C. A monochromatic beam of energy 62 keV was chosen in order to allow the acquisition of several peaks for each targeted crystallographic phase, considering the geometry of the setup. The diffracted beam was collected by a two-dimensional detector, yielding diffraction rings, which were subsequently integrated to obtain 1D diffraction patterns. This integration holds the advantage of averaging the effects of grain texture, although they are expected to be minor in the present study due to the large number of particles analysed. The acquisition rate was set to 1 image per second.

After the beginning of the data acquisition, the oven temperature was increased from 400 °C at a rate of 20 or 30 °C/min until it reached the target temperature (675 °C or 750 °C). Differences in ramp rate may affect the reaction kinetics during the heating stage; however, these will not affect the results discussed in this article. The target temperature was held until the diffraction pattern stabilised; the oven was then turned off, leading to the cooling down of the sample. Data acquisition stopped when the oven reached a temperature of 400 °C.

2.2.3. Rietveld analysis

The diffraction patterns were analysed with the software MAUD [33], based on the Rietveld refinement method [34], in order to determine the fraction of each phase detected.

The Caglioti parameters, assessing the instrumental broadening, are computed from the diffraction pattern of a reference CeO_2 sample featuring a well-known lattice parameter and a polycrystalline non-textured structure. This reference sample also allows for the determination of the X-ray wavelength with good precision.

Fig. 2.b shows an example of a diffractogram with the associated Rietveld refinement. The amorphous phase corresponding to the quartz tube was cropped out of the diffraction pattern. The liquid phase contribution was treated as background noise, which was defined as a Chebyshev polynomial with 11 fitted parameters. For all crystalline phases, a minimum of four diffraction peaks were used in the fit. The weight fraction of all phases, as well as their lattice parameters (a for cubic structures, a and c for hexagonal structures), and microstrain are obtained from the Rietveld analysis.

Based on some spectrum analyses performed manually, an automatic procedure was developed to fit all the diffraction patterns with MAUD. The quality of each fit was evaluated using the R-weighted profile value (R_{wp}) [35,36]. A Rietveld fit is considered acceptable if $R_{wp} < 10$. All the fits reported in this work satisfy this criterion. As a result, the weight fraction of each crystalline phase could be determined throughout the dealloying process.

2.3. Post mortem experiments

In order to make a link between in situ observations and the morphology and composition of resulting dealloyed particles, post mortem experiments were also conducted. Dealloyed samples were elaborated and characterised according to the following procedures.

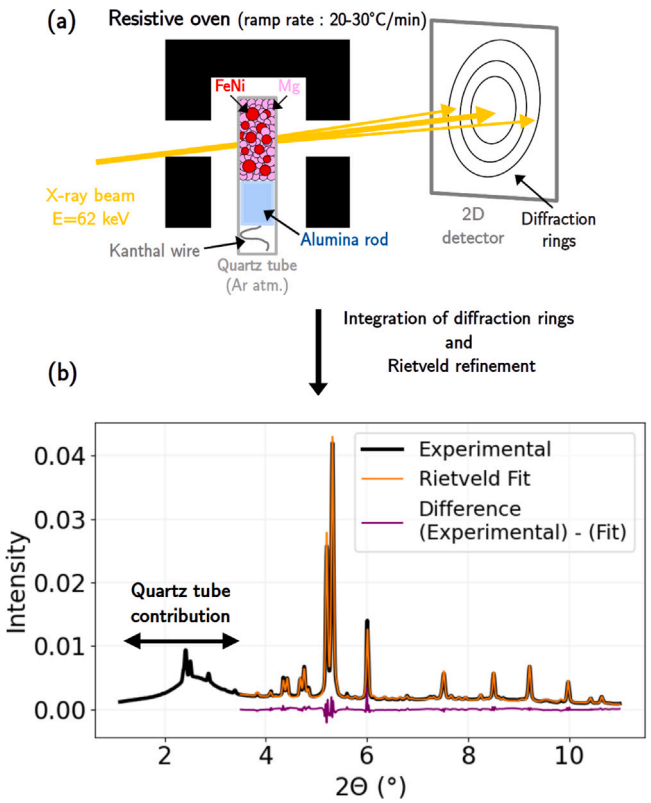

Fig. 2. (a) Schematic of the experimental setup for in situ X-ray diffraction - Beamline ID11. (b) Example of diffractogram acquired during the in situ experiment with the associated Rietveld fit. The window selected for the Rietveld fit aims at avoiding the contribution of the quartz tube.

2.3.1. Samples preparation

The raw materials used for the elaboration of the sample are identical to the ones described in Section 2.2. Invar and Mg powder were mixed manually in the same proportions as for the in situ samples. The powder mixture was inserted into a cylindrical graphite crucible (inner diameter of 10 mm) and sealed with graphite paper. The crucible was closed at both ends by two graphite pistons by applying manually a small pressure. The crucibles were then inserted in a furnace (Carbolite Gero, Germany). To remain close to the in situ experiment, a vacuum of 0.1 Pa was first achieved, before the chamber was filled with an Ar atmosphere (0.9 bar). The temperature was increased from room temperature with a ramp of 10 °C/min up to 675 or 750 °C and it was held for different durations ranging from 1 min to 1 h. The oven was then shut down and the samples were cooled down naturally inside the oven chamber. The resulting samples are cylinders measuring 10 mm in diameter and in height.

We note that, compared to the in situ experiment, the heating rate of the oven was smaller (10 °C/min versus 20 to 30 °C/min). The cooling rate could not be measured during the elaboration of these samples, but due to the larger dimensions of the sample and the high thermal inertia of the oven, the cooling stage was longer than for the in situ experiments. However, the difference between these ramp rates is not expected to have a significant influence on the resulting morphology that are primarily controlled by the duration and temperature of the temperature plateau. Therefore, in the following, the samples were considered to undergo comparable thermal treatments in both experiments. Also, no syringe was used to insert the powders into the carbon crucible, unlike the in situ case. It is worth noting that the use of a syringe might result in a discrepancy between the prepared mixture composition and the mixture actually inserted into the quartz tube, due to differences in the flowability of the Invar and Mg powders.

As a result, the composition of the initial mixture in the in situ samples and post mortem samples might differ slightly.

2.3.2. SEM characterisation

The elaborated cylindrical samples were cut and the cross-sections were prepared by Ar ion milling (IB-19530CP, JEOL, Japan), allowing to polish a surface that revealed a broad area of the dealloyed powders. The observation was performed with a scanning electron microscope (SEM, Ultra 55, Zeiss, Germany). Navigating cross-sections while observing spherical powders can be perplexing, as results may significantly differ because of the local environment. Yet, in this study, the large amount of observed powders mitigates this uncertainty. The morphology of the powders was observed through BSE imaging, and the size of the ligaments was assessed via image processing with the software ImageJ [37]. Ligaments were first isolated using the "Watershed" option and their size was analysed using the "Local Thickness" plugin on several powders visible in the cross-section. The composition of the ligaments was analysed by X-ray dispersive spectroscopy (EDX, X-flash, Bruker, US). The ligaments composition was averaged from a minimum of 25 measurements per sample, performed across various particles to mitigate the influence of local heterogeneities.

3. Results

In this section, dealloying experiments performed with target temperatures of 675 °C and 750 °C are analysed. For each temperature, we detail the phases' evolution throughout the reaction and link these results with post mortem observations. The XRD study focuses on four phases: FCC-FeNi, BCC-Fe(Ni), HCP-Mg and Mg_2Ni. Despite the fact that the formation of the Laves phase $MgNi_2$ is expected from the equilibrium phase diagram, it was not detected in any of our experiments using Invar–Mg samples. Previous studies focusing on the reaction layer between Mg and Ni samples also denoted the absence of this phase [38,39], which was attributed to a high energy barrier preventing its nucleation. Consequently, $MgNi_2$ is omitted when referring to phase equilibrium: in practice, $MgNi_2$ is excluded from the Calphad prediction of the phase diagram.[1]

Minor amounts of MgO and Mg_2Si resulting from the reaction of Mg with the quartz tube were also observed. In samples containing a large amount of Mg, these phases could represent up to 20 wt.% of the total crystalline phases whereas they remained marginal in samples featuring a smaller Mg bath. While the formation of MgO and Mg_2Si reduces the available amount of Mg for the dealloying reaction in the vicinity of the quartz tube's walls, we consider that it does not modify the reaction in the centre of the sample. Therefore, their contribution is not included in the subsequent phases analysis.

3.1. Target temperature of 675 °C

3.1.1. In situ monitoring of the process

Fig. 3.a shows the evolution of the crystalline phase fractions and the temperature evolution as a function of time for a sample InvarMg50_675. The temperature evolution is shown with a grey continuous line and the weight fraction of the different phases is shown with coloured data points. At the beginning of the experiment, the weight fractions of Invar (FCC) and Mg are equivalent, each accounting for approximately 50 wt.% of the mix. This initial state is schematically represented in Fig. 3.b. Once a temperature of 550 °C is reached, the amount of both FCC and Mg both drop and become undetectable approximately 200 s afterwards. Simultaneously, the BCC phase appears: as the Invar particles are depleted from Ni, the ligaments formed have

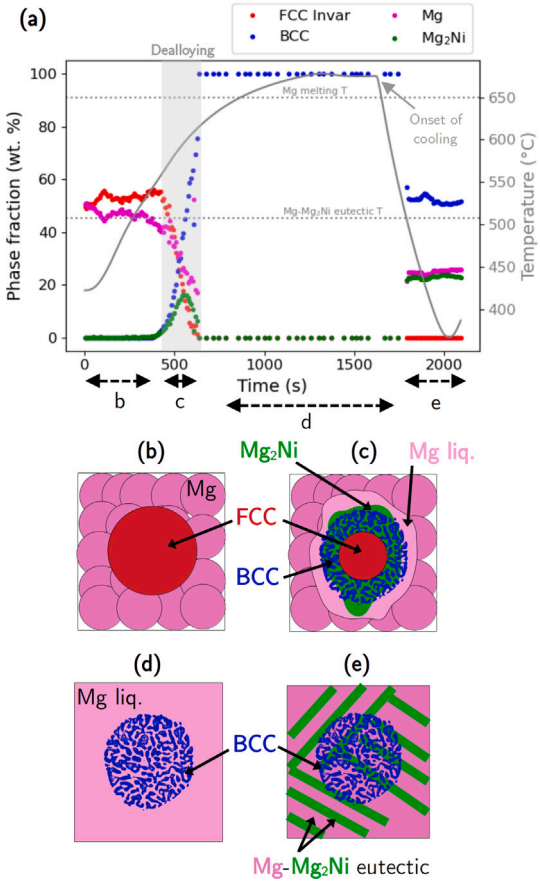

Fig. 3. Evolution of phase fractions and temperature as a function of time during the dealloying process with a target temperature of 675 °C for the InvarMg50_675 sample.

a BCC structure as schematically shown in Fig. 3.c. The transition from FCC to BCC phases visible in Fig. 3.a indicates that the dealloying reaction happens during this short period [25,30]. The dealloying period indicated by the shaded area on Fig. 4.a is defined as the time interval between the initial drop in the FCC phase fraction and its stabilisation at a lower level. During the dealloying reaction, the XRD results also demonstrate the formation of the Mg_2Ni phase that represents up to 18 wt.% of the crystalline phases before disappearing. The formation of this phase is a consequence of the dissolution of a large amount of Ni in the liquid Mg bath surrounding the Invar powders, and it is expected to appear in the vicinity of the ligaments as schematically shown in Fig. 3.c.

We note that the dealloying reaction is completed (i.e. no more FCC is detected) before reaching the melting temperature of pure Mg ($T_m^{(Mg)}$ = 650 °C). However, the onset of the dealloying reaction coincides with the melting of the Mg phase, which demonstrates the liquid-state nature of the reaction. This result can be rationalised in light of the Mg–Ni binary phase diagram (Fig. 1.b), which exhibits a eutectic at 508 °C. At the interface between FeNi and Mg powders, the interdiffusion of Ni and Mg leads to the formation of composition gradients. Such gradients allow liquid to form at a temperature below $T_m^{(Mg)}$, thereby triggering the onset of the LMD reaction.

LMD is generally considered to be controlled by liquid-state diffusion [17,40], the order of magnitude for the time t to reach a given dealloyed thickness l can be approximated by $t \sim l^2 / D_l$, D_l denoting the diffusion coefficient for Ni in liquid Mg. Previous experimental studies have demonstrated that the actual dealloying time usually falls within one order of magnitude of this rough estimate [17,40,41]. Even though D_l has not been carefully assessed experimentally, liquid metal

[1] We note that dealloying experiments carried out with $Fe_{19}Ni_{81}$ precursors during the same experimental campaign led to the formation of $MgNi_2$, indicating the requirement of a high nickel content to form this phase.

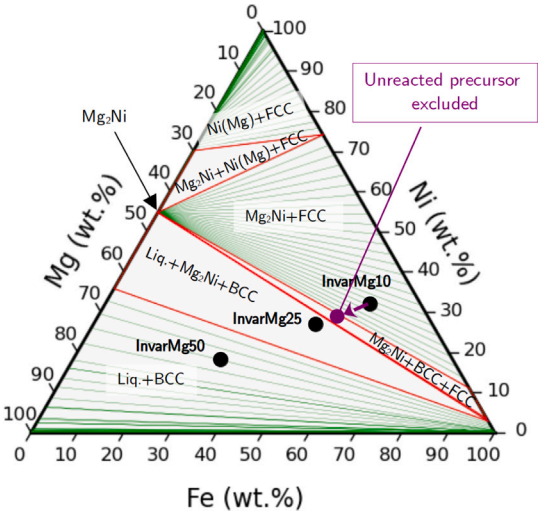

Fig. 4. Ternary FeNiMg phase diagram [23] at 675 °C displaying the global composition of the powder mixtures studied in this section. For the sample InvarMg10_675, the composition of the purple dot excludes the fraction of the precursor that did not react with Mg. The $MgNi_2$ phase was ignored as it was not observed during the XRD acquisition.

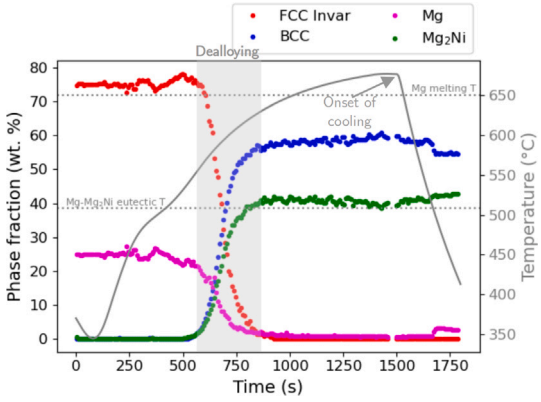

Fig. 5. Evolution of phase fractions and temperature as a function of time during the dealloying process with a target temperature of 675 °C for the InvarMg25_675 sample.

diffusion coefficients are of the order of $D_l = 10^{-9}$ m^2/s [42], yielding $t \sim 0.1$ s for $l = 10$ μm. Hence, considering the dimensions of our powders ($d_{90v} = 15$ μm), dealloying should be completed in a few seconds at most, which is two orders of magnitude faster than observed in our experiment. This suggests that the progressive melting of Mg seen in Fig. 3.a is the rate-limiting process in the present dealloying reaction. The LMD reaction can occur if liquid Mg is available, but its melting is not instantaneous. It is initiated around 550 °C, concurrently with the onset of the dealloying reaction, and progresses as the temperature increases, and as Ni comes in contact with solid Mg, allowing its melting. Dealloying kinetics may also be slowed down by the presence of the solid phase Mg_2Ni that forms around the ligaments during the dealloying reaction and that could impede the diffusion of Ni in liquid Mg.

The Mg_2Ni phase rapidly dissolves with the temperature rise, giving way to a single crystalline BCC phase coexisting with liquid Mg containing the dealloyed Ni, as schematically represented in Fig. 3.d. Such equilibrium can be compared to the prediction of the ternary phase diagram at 675 °C represented in Fig. 4. The sample discussed here contains a large amount of Mg and its composition is represented by the black dot labelled "InvarMg50" on the ternary phase diagram: the phase diagram predicts an equilibrium between a BCC Fe-rich phase and a Mg liquid containing around 25wt.% of Ni. In particular, the Mg_2Ni phase is not expected to be at equilibrium at 675 °C for this sample. The XRD results are therefore consistent with the phase diagram prediction.

During the cooling process, the liquid phase solidifies around a temperature of 510 °C, forming Mg and Mg_2Ni phases in a eutectic structure as schematically represented in Fig. 3.e. After cooling, the BCC phase represents a large fraction of the sample, while no FCC phase is detected. This complete transition from FCC to BCC suggests that all the Invar powders were successfully dealloyed. Upon cooling, the diffraction rings corresponding to the Mg_2Ni phase appear "spotty", indicating the formation of a few large grains. Therefore, the applied Rietveld analysis does not provide a precise quantification of the phases after cooling, as the grains are no longer numerous and randomly oriented.

Fig. 5 displays the evolution of phase fractions for another sample, InvarMg25_675, with a decreased amount of Mg compared to InvarMg50_675. The beginning of the reaction is similar to the first case: the FCC phase completely transforms into BCC while Mg melts. Concurrently with these transformations, the Mg_2Ni phase appears as in the previous case; however, in this instance, the Mg_2Ni phase remains throughout the reaction, resulting in the coexistence of the BCC phase with Mg_2Ni. The global composition of the initial powder mixture, as displayed on the ternary phase diagram (Fig. 4), consistently predicts a ternary equilibrium between BCC, liquid and Mg_2Ni. The presence of a small amount of liquid Mg is confirmed during the cooling step, as a detectable amount of crystalline Mg appears on the diffraction pattern. The absence of FCC phase at the end of the reaction also confirms that the Invar powders are completely dealloyed during the reaction.

In the two previous samples, the size of the Mg bath is large enough to allow complete dealloying. The third case discussed below involves a powder mixture containing a limited amount of Mg, that represents 10 wt.% of the initial sample. Fig. 6.a shows the phases evolution for this InvarMg10_675 sample heated to a target temperature of 675 °C. Like for the previous cases, the dealloying reaction starts at 550 °C: the amount of FCC drops while the formation of BCC and Mg_2Ni is detected, showing the formation of BCC Fe-rich ligaments and Mg_2Ni as a consequence of the dealloying reaction, as schematically shown in Fig. 6.c. This reaction occurs during a time period of approximately 200 s identified on the graph.

As shown in Fig. 6.a, three phases remain after the dealloying reaction: FCC, BCC and Mg_2Ni. A slow transition from BCC to FCC is visible during the temperature plateau, suggesting that the BCC ligaments are undergoing a transition towards an FCC structure (Fig. 6.d). Because of this transition, the detected FCC phase includes contributions from both undealloyed Invar and ligaments that have transformed into an FCC structure. Since Fe and Ni have very similar atomic radii, the lattice parameters of FCC Invar and the ligaments (richer in Fe) are too close to be distinguished. As a result, the corresponding peaks were fitted as a single FCC phase denoted "FCC Invar + Lig." in Fig. 6. In the initial stages of the reaction, the formation of BCC ligaments can be explained by the lower temperature and the contact of the ligaments with pure Mg. However, as the temperature and the amount of Ni in the liquid bath increase, equilibrium conditions shift in favour of FCC ligaments.

As seen in Fig. 6.d, most of the FCC phase remains unaffected by the dealloying reaction. This fraction of FCC corresponds to the undealloyed precursor and the equilibrium reached at the end of the reaction is not defined by the overall initial composition of the powder mixture. Thus, it would be hazardous to consider the total composition of the mixture to predict the phase equilibrium. By excluding the amount of unreacted precursor (corresponding to the remaining FCC after the end of the dealloying reaction) from the total composition, the composition to be considered is represented by a purple dot in Fig. 4. It falls in the ternary equilibrium region Mg_2Ni + BCC + FCC, rationalising the transformation of the ligaments to an FCC structure.

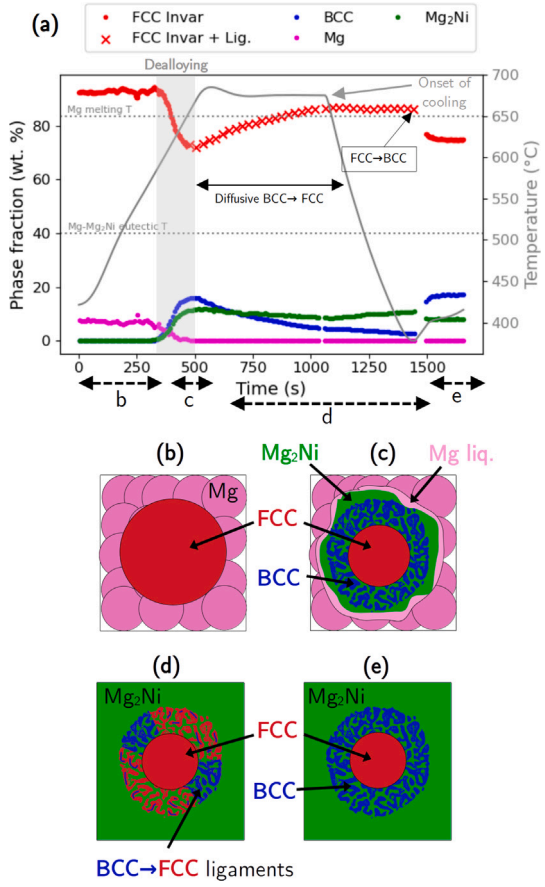

Fig. 6. Evolution of phase fractions and temperature vs. time during the dealloying process with a targeted temperature of 675 °C for the InvarMg10_675 sample.

Such transformation goes along with the enrichment of the ligaments in Ni. Concurrently with the BCC → FCC transition, the fraction of Mg_2Ni slightly decreases, suggesting that Ni could originate from this phase. Simultaneously, some Mg would be released as well, enabling the dealloying reaction to continue marginally. Another possibility is the diffusion of Ni from the undealloyed precursor into the ligaments. Both these processes involve solid-state diffusion of Ni, which explains the slow kinetics of the transformation.

Upon cooling, a fast FCC to BCC transition is visible on Fig. 6.a; the fraction of FCC reverts to the amount observed immediately after the dealloying reaction, suggesting that the FCC ligaments are not stable upon cooling. The fast kinetics of this transition indicates that it might be mediated by the martensitic transformation in FeNi alloys [43,44]. In addition, the amount of Mg_2Ni remains almost unchanged during the cooling stage and the amount of crystalline Mg seems to be undetectable. This suggests that the initial amount of Mg is entirely replaced by Mg_2Ni upon the dissolution of Ni from the Invar powders (see Fig. 6.d-e).

In this case, only a fraction of the initial powders undergo dealloying, leading to the formation of BCC ligaments. These ligaments subsequently transform into thermodynamically favoured FCC ligaments and eventually revert to a BCC structure upon cooling. However, during the process, a large part of the FCC phase, corresponding to the initial precursor (Invar), remained unaffected by the reaction. This suggests that the powders display a partially dealloyed structure as discussed in the next section.

3.1.2. Comparison with post mortem experiments

Figs. 3 and 6 reveal two different scenarios for samples heated to 675 °C, depending on the initial composition of the powder mixture. In order to link each case to the resulting morphology of the dealloyed powders, samples were elaborated in similar conditions as for the in situ experiments and observed post mortem.

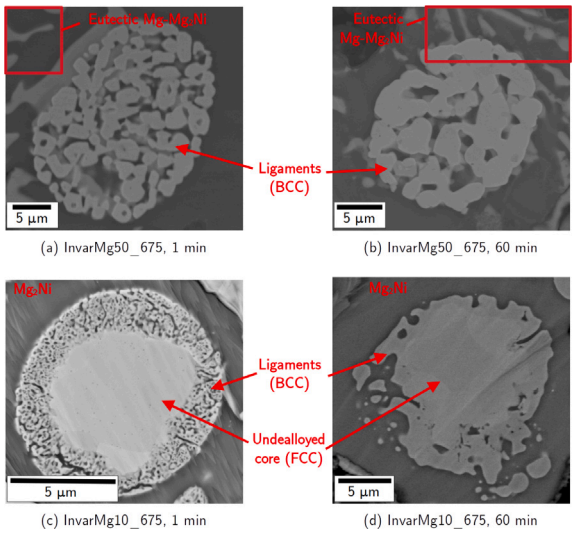

Fig. 7. SEM-BSE images of powders heated to 675 °C with varying compositions and dealloying times.

Fig. 7.a and b show the cross-sections of representative particles of InvarMg50_675 heated to 675 °C after a temperature plateau of 1 min and 1 h respectively. As expected from the in situ analysis, these images reveal the complete dealloying of the powders, from their periphery to their core. Typical eutectic Mg–Mg_2Ni microstructure is also visible in both images, resulting from the solidification of the Mg bath enriched in Ni. These observations are in agreement with the analysis of in situ results (Fig. 3).

Fig. 7.c and d show cross-section images for InvarMg10_675 samples obtained after dealloying times of 1 min and 1 h, in relation with the in situ experiment shown in Fig. 6. In contrast with the dealloyed microstructures shown in Fig. 7.a and b, Fig. 7.c and d show that the powders are partially dealloyed. Their core remained unaffected by the dealloying reaction, as confirmed by EDX results revealing a composition identical to the Invar precursor ($Fe_{65}Ni_{35}$) in the centre of the particles. However, the periphery of the powders exhibits porous structures, indicating the onset of the dealloying reaction. Interestingly, these particles are embedded into Mg_2Ni phase, and no crystalline Mg could be detected in their vicinity. This observation implies the absence of liquid at high temperature, otherwise, some eutectic Mg–Mg_2Ni structure would be visible. Again, these post mortem observations corroborate the results from in situ experiments shown in Section 3.1.1.

The micrographs shown in Fig. 7 also prompt a discussion on the coarsening of the ligament structure that accompanies and follows the dealloying reaction. It refers to the reduction of the total area of the porous structure that results in an increase of the ligaments size [40,45]. For the samples dealloyed in a large Mg bath (InvarMg50_675), the ligaments size was estimated to 1.2 µm for the 1 min sample (Fig. 7.a) and 1.8 µm for the 60 min dealloyed sample (Fig. 7.b). Regarding the InvarMg10_675 involving a small Mg bath, powders dealloyed for 1 min (Fig. 7.c) exhibit the thinnest ligaments structure, making it difficult to quantify the ligaments size. The formation of Mg_2Ni around the particles could explain the thin ligament structure as its presence might hinder the diffusive process enabling coarsening of the ligaments. In Fig. 7.d, powders dealloyed for 60 min exhibit a very rough surface due to the extended coarsening time. However, the core–shell structure is still clearly visible.

In addition to the samples' microstructure, the composition of the ligaments resulting from the dealloyed reaction could be probed by

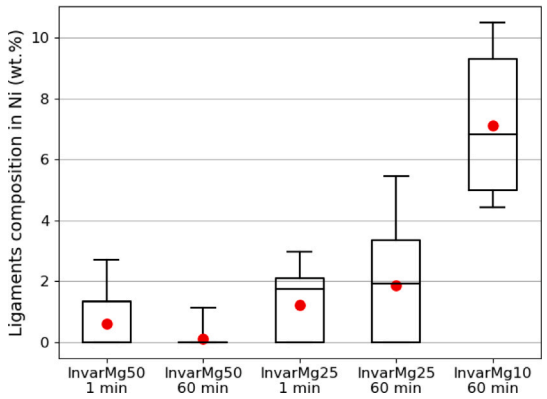

Fig. 8. Ligaments composition in Ni for Invar samples heated to 675 °C with varying dealloying conditions (time, initial mixture composition). For each sample, the box plot displays the minimum and maximum values, the first and third quartiles, and the median value. Red dots indicate the average ligaments composition.

EDX. Fig. 8 reports the distribution of the ligaments composition with a box plot, as well as their averaged composition for dealloyed powders at 675 °C for 1 min and 60 min, with varying initial powders mixtures. The ligaments of the sample InvarMg10_675 held at high temperature for 1 min being very thin (see Fig. 7.c), their composition could not be probed using SEM-EDX.

InvarMg50_675 exhibits ligaments with very small amounts of Ni. InvarMg25_675 features an average ligament composition of 2 wt.% of Ni. Regarding the sample InvarMg10_675 with the smaller Mg bath, the average ligaments composition is around 7 wt.%. However, for this latter sample, the ligaments composition is heterogeneous and ranges from 4.5 wt.% Ni to 10.5 wt.% Ni. Such a high content of Ni should result in the formation of FCC ligaments at 675 °C according to the Fe–Ni phase diagram (see Fig. 1.a). However, Fig. 6 indicates that all the ligaments revert to a BCC structure during the cooling stage. This is attributed to the martensitic transformation of $Fe_{1-x}Ni_x$ alloys upon cooling reported in the literature for Ni content satisfying $5 < x < 25$ (wt.%) [43,44].

Fig. 8 reveals a clear correlation between the initial amount of Mg powders and the ligament composition resulting from the dealloying reaction: samples with a smaller Mg bath tend to feature ligaments with a higher Ni content. Indeed, increasing the amount of precursor tends to shift the system towards equilibria in the upper part of the phase diagram shown in Fig. 4, thereby favouring ligaments richer in Ni. In these samples, no notable effect of the reaction time was observed on the ligaments composition.

The post mortem observations reported in this section reveal that the ratio between precursor and Mg powders influences both the dealloying ratio and the composition of the ligaments.

3.2. *Target temperature of* 750 °C

In a second set of experiments, dealloying was conducted at a temperature of 750 °C in order to explore the influence of temperature on the equilibrium conditions. As in the previous section, samples are analysed with in situ XRD monitoring and post mortem SEM observations.

3.2.1. *In situ analysis*

Fig. 9 exhibits the evolution of phase fractions throughout the reaction for two different powder mixtures InvarMg50_750 and InvarMg30_750.

Fig. 9.a displays the case of a large Mg bath (InvarMg50_750). Here, the dealloying reaction again occurs below $T_m^{(Mg)}$. Upon heating, the particles are dealloyed entirely as testified by the transition from FCC

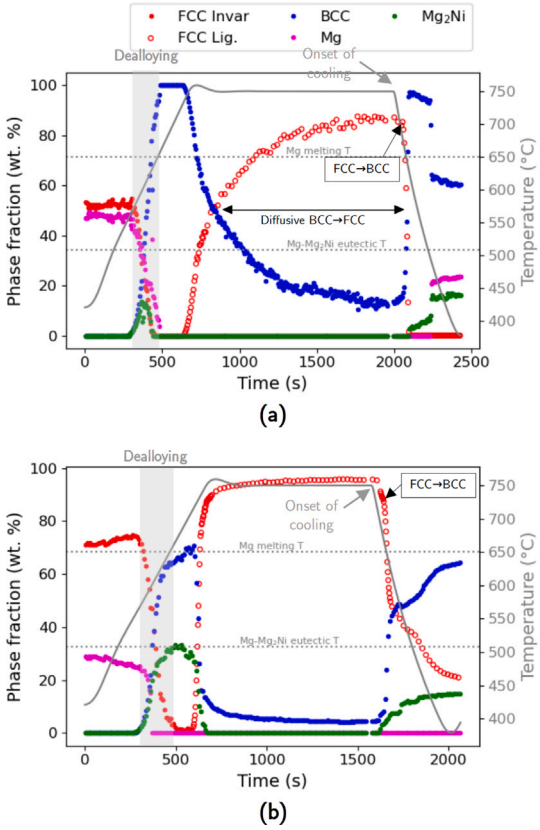

Fig. 9. Evolution of phase fractions and temperature vs. time during the dealloying process with a target temperature of 750 °C. (a) InvarMg50_750. (b) InvarMg30_750.

to BCC phases. Similarly, as in Fig. 3, some Mg_2Ni briefly appears before dissolving into the Mg bath. After the completion of the dealloying reaction, at a temperature of 740 °C, the BCC ligaments slowly transform to an FCC structure. This phenomenon was not observed at a temperature of 675 °C for the same amount of Mg (Fig. 3). After 2000 s, a majority of the ligaments exhibit an FCC structure. The composition of the mix is shown on the phase diagram of Fig. 10 and suggests an equilibrium between Mg(Ni) liquid and Fe-rich BCC ligaments. However, the composition of the mix is close to the Liq.+BCC+FCC ternary equilibrium, such that small uncertainties on the composition of the mix[2] could lead to the formation of FCC ligaments in equilibrium with Mg(Ni) liquid. Upon cooling, a quick transition from FCC to BCC is observed before the eutectic solidification of the Mg–Ni liquid takes place.

In Fig. 9.b, the sample InvarMg30_750 contains a lower amount of Mg (approximately 30 wt.%). However, this amount appears to be sufficient to fully dealloy the particles as the fraction of FCC drops to zero after the dealloying reaction. After the dealloying period, the amount of Mg_2Ni decreases slightly, transforming back into liquid Mg. Because only solid phases are detected and quantified, the melting of Mg_2Ni leads to an increase of the BCC phase fraction. This increase is therefore not related to the continuation of the dealloying reaction.

In a second step, the BCC ligaments undergo a transition towards an FCC structure. Such transition is in agreement with the phase diagram (see Fig. 10) that predicts an equilibrium between liquid Mg(Ni) and FCC ligaments containing approximately 10% of Ni. This transition is significantly faster than the one visible in Fig. 9.a, which might be a

[2] The formation of MgO and Mg_2Si close to the quartz tube might reduce the amount of available Mg for the reaction

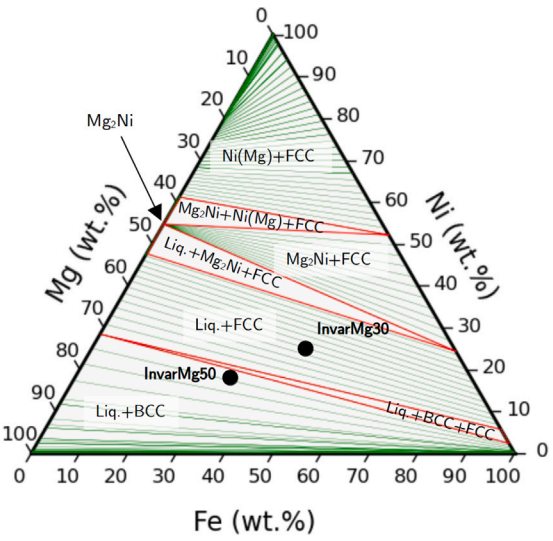

Fig. 10. Ternary FeNiMg phase diagram [23] at 750 °C displaying the global composition of the powder mixtures studied in this section. The $MgNi_2$ phase was ignored as it was not observed during the XRD acquisition.

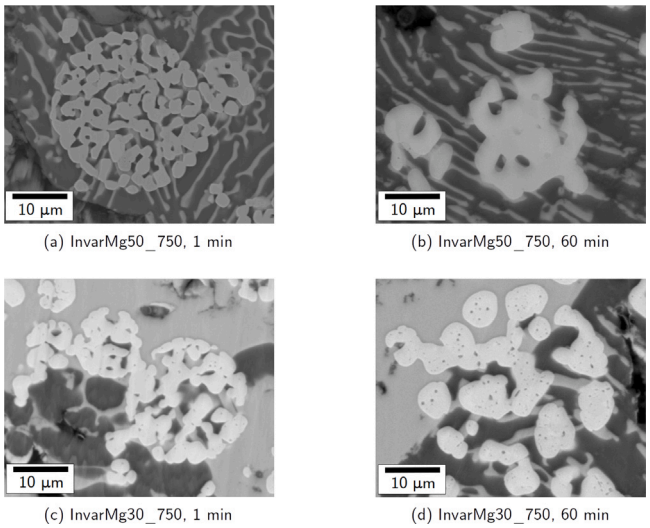

Fig. 11. SEM-BSE images of powders heated to 750 °C with varying compositions and dealloying times.

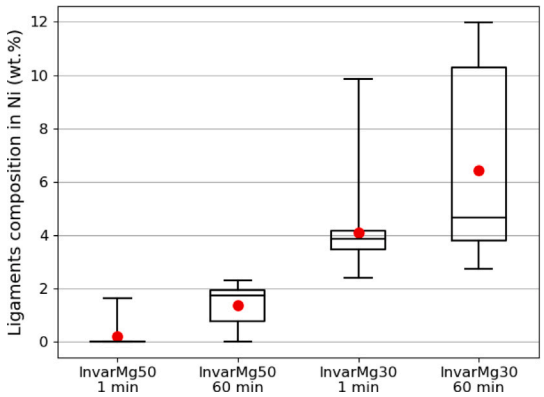

Fig. 12. Ligaments composition in Ni for several dealloyed Invar samples at 750 °C with varying dealloying conditions (time, initial mixture composition). For each sample, the box plot displays the minimum and maximum values, the first and third quartiles and the median value. Red dots indicated the average ligaments composition.

consequence of a stronger driving force. InvarMg50_750 (Fig. 9.a) falls in a region of the phase diagram where the system is on the verge of stability of both BCC and FCC phases. Therefore, the driving force for the BCC to FCC transition may be lower in this case.

3.2.2. Post mortem observations

Samples are elaborated in similar conditions as in the in situ experiments with a target temperature of 750 °C. Fig. 11 shows post mortem SEM observations of the dealloyed samples. As expected from the in situ analysis, all powders exhibit a fully dealloyed structure with a significant coarsening for the sample kept at 750 °C for 60 min. The microstructure of the solidified baths of the InvarMg50_750 and InvarMg30_750 samples also differs. On Fig. 11.a and b, eutectic microstructures resulting from the solidification of the Mg(Ni) liquid are clearly visible. The samples also display a large area of solidified Mg. On the other hand, InvarMg30_750 samples shown on Fig. 11.c and d exhibit eutectic zones along with large Mg_2Ni platelets. This is attributed to the higher Ni content in the smaller Mg bath. According to the Mg–Ni phase diagram (Fig. 1.b), a hypoeutectic composition of the bath (less than 23 wt.% Ni) should lead to the formation of Mg and Mg–Mg_2Ni eutectic (as seen in the case of InvarMg50_750). On the other hand, a hypereutectic composition should result in the formation of Mg_2Ni and Mg–Mg_2Ni eutectic (as observed in the case of InvarMg30_750). As stated in the previous section, this higher composition of the bath in Ni suggests that ligaments should consequently exhibit a higher composition in Ni according to the ternary phase diagram (Fig. 10). To confirm this assumption, EDX measurements were performed.

Fig. 12 shows the ligaments composition distribution of the various samples along with the average ligaments composition. The ligaments of the sample InvarMg50_750, dealloyed in a large Mg bath, display an undetectable amount of Ni after a 1 min reaction. After a 60 min reaction, they contain an average of 1.4 wt.%Ni. With such a composition, these ligaments should have a BCC structure at high temperatures according to the Fe–Ni phase diagram Fig. 1.a. However, it is plausible that these ligaments had a higher Ni composition at high temperatures, leading to their transformation into an FCC structure. Some Ni may be released into the bath upon cooling, resulting in a decrease in the final Ni composition of the ligaments. Another potential explanation for this discrepancy could be the difference between the initial mixture composition of the in situ and the post mortem samples as explained in Section 2.3.1, which could result in different compositions of the ligaments.

The InvarMg30_750 sample exhibits a higher Ni content in the ligaments, supposedly due to the bath that also had a higher Ni content as suggested above. An average close to 4 wt.%Ni was measured in the sample held at 750 °C for 1 min. Regarding the sample with a temperature plateau of 60 min, the ligaments composition seems to be heterogeneous, with ligaments exhibiting a composition around 4 wt.%Ni and others around 10 wt.%Ni, yielding an average composition close to 6 wt.%. These heterogeneities are expected to appear during the cooling stage: according to the Fe–Ni phase diagram (Fig. 1.a), FCC ligaments enriched in Ni (more than 6 wt.%Ni at 750 °C) decompose into Ni-rich FCC ligaments and Ni-poor BCC ligaments upon cooling.

Several conclusions can be drawn from these EDX measurements. First, they corroborate the prediction of the phase diagram: like in the case at 675 °C, a lower amount of Mg in the initial mixture leads to the formation of ligaments richer in Ni, as shown by the phase diagram. Secondly, increasing the temperature to 750 °C favours the formation of FCC ligaments that could retain their structure after cooling as observed for the sample InvarMg30_750 held at high temperature for 60 min, consistently with the phase evolution shown in Fig. 9.b.

3.2.3. Evolution of the lattice parameter of the FCC phase

As shown in Section 3.2.1, the samples heated to 750 °C exhibit FCC ligaments. Section 3.2.2 showed that the ligaments composition obtained from post mortem measurements highly depends on the initial mixture composition. Moreover, the composition of ligaments influence the lattice parameter of the FCC phase. Therefore, it is possible to use the measure of the lattice parameter obtained from the Rietveld refinement of the XRD spectra as an indirect in situ measurement of the composition of ligaments.

Fig. 13 illustrates the variation of the lattice parameter a of the FCC phase with respect to pure Invar at the same temperature (i.e. $\frac{a_{FCC}(T)-a_{Invar}(T)}{a_{Invar}(T)}$) as a function of time. The temperature evolution is also displayed on the same figure. The change of the lattice parameter of pure Invar with respect to the temperature is fitted with a linear relationship. Therefore, this figure allows to follow the deviation of the lattice parameter with respect to Invar to emphasise changes in the composition of the FCC structure. The analysis was performed for the samples InvarMg50_750 and InvarMg30_750. As shown in the previous sections, these samples were completely dealloyed, such that the FCC phase forming after the dealloying reaction corresponds necessarily to the Fe-rich ligaments.

During the heating stage, the FCC phases of both samples exhibit a lattice parameter equal to that of pure Invar since the precursor powders have not been dealloyed yet. When reaching a temperature close to 600 °C, the FCC peaks completely disappeared from the diffraction pattern. An FCC phase appear again around 715 °C for the InvarMg30_750 sample and 735 °C for the InvarMg50_750 sample, allowing to resume the monitoring of the FCC lattice parameter. Both FCC phases have a larger lattice parameter than Invar and comparatively, the FCC phase in InvarMg50_750 exhibits a larger lattice parameter than in InvarMg30_750.

Despite the small atomic size difference between Fe and Ni atoms, the lattice parameter of FCC FeNi alloys decreases for increasing content in Ni [46,47]. This trend is also consistent with predictions obtained with the Thermo-Calc database TCFE10 [29].

Therefore, the results shown in Fig. 13 reveal that the FCC ligaments resulting from the dealloying of InvarMg30_750 contain more Ni than the ones forming in InvarMg50_750. This is consistent with the thermodynamic equilibrium expected from the phase diagram at 750 °C (see Fig. 10). In addition, this result is also in agreement with the post mortem EDX experiments discussed in the previous section.

During the temperature plateau, an enrichment of the ligaments composition in Ni is expected as suggested by Fig. 12, which should result in a decrease of the lattice parameter. Such a trend is however not visible in Fig. 13. This could be explained by the relatively short temperature plateau used in the in situ experiments compared to the 60 min temperature hold subjected to the samples used for post mortem SEM experiments.

4. Discussion

The results detailed in the previous section reveals the influence of the dealloying parameters on the resulting microstructure and ligament composition. We show in particular that the results are consistent with the predictions of the phase diagrams.

A similar approach was considered by Wada et al. [14] who showed that changing the composition of the Mg bath by adding Bi allows to modify the thermodynamic equilibria and consequently the ligaments composition. In the present study, the influence of two other parameters was investigated: the temperature (675 °C and 750 °C) and the size of the bath (i.e. the amount of Mg in the initial powder mixture). Compared to dealloying experiments performed on large samples as in Ref. [14], this latter parameter is easily adjustable in our experiments involving powders. Both parameters allowed to change the thermodynamics of the system and to explore equilibria in the FeNiMg ternary phase diagram.

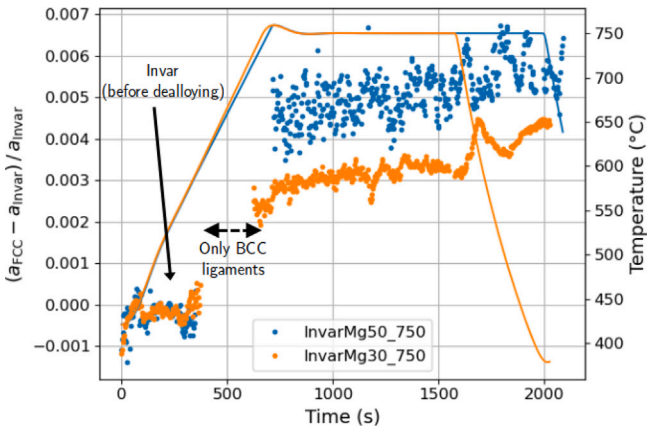

Fig. 13. Variation of the lattice parameter and temperature as a function of time. The lattice parameter was determined from the diffraction peaks corresponding to the FCC phase using the Rietveld method.

4.1. In situ XRD to clarify the kinetics and thermodynamics of dealloying

In situ XRD observations allowed us to spot a two-step reaction. In a first step, the dealloying reaction stops after 100–200 s. The system then continues to react and gets closer to equilibrium conditions through diffusion and phase transformations.

4.1.1. Kinetics of the dealloying reaction

In a first step, all the samples for which the reaction has been monitored showed a dealloying reaction starting around 550 °C, identified by the drop of the FCC phase and the formation of a BCC phase. In all cases, this transformation stopped even below the melting temperature of Mg ($T_m^{(Mg)}$ = 650 °C), showing the completion of the dealloying reaction. This early reaction is due to the Mg–Ni eutectic that allows the formation of liquid from temperatures as low as 508 °C. This leads to the dealloying reaction occurring at a slower rate than liquid diffusion-controlled reactions. In our scenario, the reaction was constrained by the gradual melting of the Mg powders.

In typical dealloying experiments with large samples, controlling the dealloying thickness is possible by adjusting the immersion time of the precursor. In situ experiments have shown that due to the small size of powders, the dealloying reaction finishes within 200 s. Given the slow heating and cooling rates, controlling the dealloying fraction of the particles by stopping the dealloying reaction appears challenging. Other techniques allow fast heating rates and short dealloying times such as selective laser melting [20,48]. In Ref. [20], these brief dealloying reactions have been compared to longer experiments conducted in a furnace and yielded very thin (~ 100 nm) ligament structures for TaTi powders dealloyed in Cu. Although this technique does not allow precise control of the temperature and may result in uneven heating, it opens up new possibilities for manipulating the dealloying morphology, particularly the dealloying thickness. Also, relying on solid-state dealloying [49,50], owing to its slow kinetics limited by solid state diffusion, could offer appropriate control of the dealloying depth for powder particles, as well as a limited coarsening rate and therefore, thinner ligaments.

4.1.2. Approaching equilibrium conditions

In a second step, the phases present in the system evolve towards the equilibrium conditions that depend on the composition of the powder mixture and on the temperature. In the present case of a slow temperature ramp, we can have a good control on this second step.

Phase diagrams appeared to be an efficient tool to predict the phase transformations occurring after the dealloying reaction. With a large Mg bath, the initial mixture goes towards its equilibrium composition where liquid Mg containing Ni is at equilibrium with BCC or FCC

ligaments depending on the composition and temperature conditions (see Figs. 3 and 9.a). Conversely, a smaller Mg bath brings the system towards regions of the phase diagram (see Fig. 6) where FCC ligaments containing a residual amount of Ni are at equilibrium with solid Mg_2Ni.

The in situ observations also gave insights into the phenomena leading to the resulting morphologies observed post mortem. Firstly, it helped to clarify the role of intermetallic phases, particularly Mg_2Ni, in the dealloying reaction. Mg_2Ni consistently nucleates during the process, but its persistence or disappearance depends on the temperature and composition conditions. As a solid phase, Mg_2Ni may influence the kinetics of the dealloying reaction. Notably, within this study, the thinnest microstructure was observed in the samples labelled InvarMg10_675 (Fig. 7.b), held at 675 °C for 1 min. Here, Mg_2Ni persisted after the dealloying reaction. The solid environment around the dealloyed powders hinders the coarsening mechanism, resulting in thin ligaments. This slow coarsening is similar to that observed in solid-state dealloying, where the process relies solely on solid-state diffusion, leading to decreased kinetics [49]. Dealloying in a small liquid bath can be viewed as an intermediate process between liquid metal dealloying and solid-state dealloying: initially, the liquid bath facilitates rapid kinetics, but as time progresses, it is gradually replaced by Mg_2Ni, consequently slowing both the dealloying process and the coarsening. On the other hand, dealloying within a large Mg bath resembles typical reactions found in model systems (like TaTiCu [17,51] or NiCuAg [18], etc.) where a unique solid phase reaches equilibrium with the liquid phase at high temperature.

Similarly, the Mg_2Ni phase formed early in the dealloying process (see Fig. 3 and 9), might impact the kinetics of the dealloying reaction before disappearing.

4.2. Towards the design of controlled dealloyed structure based on thermodynamics

As described above, tuning the dealloying parameters investigated here (temperature and size of the bath) allows to change the equilibrium conditions of the system. Hence, adjusting these parameters appropriately may allow to design dealloyed powders with controlled features.

First, decreasing the size of the bath appears as a good tool to control the dealloying thickness of the particles [20]. Once the bath cannot accept more of the sacrificial element, the dealloying reaction spontaneously stops, yielding a core–shell structure as observed for sample InvarMg10_675 (see Fig. 7.c and 7.d) . Our analysis of the reaction reveals that the dealloying capacity of Mg goes beyond the solubility limit of Ni in liquid Mg (which is 20 wt.%Ni at 675 °C) as evidenced by the absence of liquid Mg and the coexistence of FCC and Mg_2Ni at high temperatures (see Fig. 6). The dealloying reaction stops when liquid Mg is replaced by Mg_2Ni. In other words, two Mg atoms can accept up to one Ni atom. In these situations, the Fe-rich ligaments contain a residual amount of Ni that approaches a thermodynamic equilibrium condition with Mg_2Ni.

To formalise this reasoning, let us consider a precursor $Fe_{1-x}Ni_x$, and the formation of ligaments with composition $Fe_{1-y}Ni_y$ in equilibrium with the surrounding Mg_2Ni after dealloying. For simplicity reasons, the difference in molar mass between Fe and Ni is neglected such that x and y are assimilated to atomic fraction. We denote $\phi_{mix} = m_{Mg}/m_{prec}$ the mass ratio of Mg and precursor powders. Assuming that the dealloying reaction stops when liquid Mg is replaced by Mg_2Ni, the fraction of precursor undergoing the dealloying reaction is given by:

$$\phi_{dealloyed} = \phi_{mix} \frac{M_{Ni}}{2(x-y)M_{Mg}} \quad (1)$$

where $M_{Ni} = 58.7\,g/mol$ and $M_{Mg} = 24.3\,g/mol$ are the molar masses of Ni and Mg. A value $\phi_{dealloyed} > 1$ means that the amount of Mg is sufficient to fully dealloy the precursor.

As an example, for InvarMg10_675 sample, the phase quantification before the onset of the dealloying reaction reveals that $\phi_{mix} \simeq 0.07$. Assuming that after dealloying, the ligaments retain an amount $y = 7\%$ of Ni (as observed in post mortem measurements), Eq. (1) gives $\phi_{dealloyed} = 0.30$. Experimentally, the dealloyed fraction can be estimated by comparing the amount of the FCC phase before and after the reaction, resulting in $\phi^{exp}_{dealloyed} = 0.22$. Both numbers are in satisfactory agreement and the difference between them can be attributed to measurement uncertainties and to the formation of Mg_2Si and MgO compounds in the experiments that reduces the amount of Mg available for the dealloying reaction.

Secondly, modifying the equilibria is a powerful tool to control the crystal structure of the ligaments. Ligaments enriched in Ni tend to adopt an FCC structure that can be desirable as it provides better ductility and formability than BCC alloys, which are key properties in coating applications such as cold spray [52]. Our results show that this amount of Ni can be controlled through adjustments in both bath size and temperature, provided that sufficient time is allowed for the system to approach equilibrium conditions.

Thirdly, the size of the ligaments also depends on the elaboration conditions. The unavoidable coarsening phenomenon resulting in thicker ligaments, is known to depend on temperature and reaction time [30,40]. Our study also shows that the initial mixture composition influences the coarsening. In particular, a small amount of Mg leads to particles embedded in solid Mg_2Ni, limiting the coarsening phenomenon (see Fig. 7.c). If the exposure at high temperature is long, the coarsening phenomenon can result in very rough structures, as depicted in Fig. 7.d.

It is also essential to discuss the limitations of relying on thermodynamic equilibrium to design dealloyed structures. To begin with, the ternary phase diagrams we referred to in Section 3 were simplified by ignoring the phase $MgNi_2$ as it was not observed experimentally even though its formation is predicted by equilibrium thermodynamics. Therefore, when generalising these findings to other systems, one has to be cautious about relying on equilibrium phase diagrams to design porous powders.

Moreover, all the controllable features mentioned above (ligaments size, composition, crystal structure and dealloyed fraction) are interconnected. Hence, it seems difficult to obtain core–shell structures featuring ligaments without Ni. Approaching equilibrium conditions to enrich ligaments in Ni has been shown to require time, but time also causes coarsening that may result in very coarse microstructures (see Fig. 7.d) detrimental for many applications of dealloyed materials. Therefore, identifying optimised parameters is necessary to achieve the desired characteristics for the dealloyed powders.

Also, the structures obtained at high temperature are shown to be modified by the cooling stage. In particular, FCC phases may transform to BCC if their content in Ni is not high enough. Additionally, slow cooling facilitates diffusion which might alter the composition of the ligaments. Such transformations could be hindered by rapid quenching of the samples.

5. Conclusion

In this study, the liquid metal dealloying reaction of FeNi powders in liquid Mg has been monitored by in situ X-ray diffraction performed at the European Synchrotron Radiation Facility on the Beamline ID11. This experiment allowed us to unveil the different phase changes taking place during the dealloying reaction. We rationalise these results by considering the phase diagram of the FeNiMg system. In addition, the in situ results are shown to be systematically consistent with post mortem observations. Armed with a deeper understanding of the dealloying reaction of the FeNiMg system, we suggest strategies to better control morphologies and compositions of the dealloyed powders. The main findings are summarised as follows:

1. Liquid metal dealloying of powders was successfully monitored under a good control of temperature, XRD allowed to capture both kinetics and phase transformations involved during LMD. The effect of the different steps (temperature ramp, temperature plateau, cooling) could be distinguished.
2. The size of the bath appeared to be an easily adjustable parameter to efficiently control the dealloying thickness, yielding dealloyed particles with core–shell structures in some conditions.
3. Modifying the phase equilibria by changing the parameters of the dealloying reaction (bath size and temperature), provides an effective means to tune the microstructure of the dealloyed powders. In particular, it allows controlling the composition and crystalline structure (BCC or FCC) of the ligaments within the dealloyed powders.
4. The effect of intermetallic phases on the dealloying reaction was clarified. Although predicted by the phase diagram, $MgNi_2$ did not nucleate in our experiments probably due to a high energy barrier to overcome for nucleation. However, Mg_2Ni was observed, and the conditions allowing its presence were elucidated. As a solid phase, it may decrease the dealloying kinetics. By impeding the coarsening phenomenon, it was also identified as the cause of the very thin ligament structures that could be observed post mortem.

The current study sets the stage for the widespread application of thermodynamic data to enhance the control and design of dealloyed structures. Approaches addressing the limitations of our experimental setup have been discussed and warrant future work, including solid-state dealloying, brief laser-induced melting, and quenching to mitigate cooling effects.

Ultimately, the development of dealloyed powders can be approached with an application-oriented perspective. Tailoring porous powders to meet mechanical requirements opens avenues for their use as base materials in coating or additive manufacturing applications. Earlier research has explored the application of porous powders [53,54] and core–shell particles [55,56] in cold spray applications. These studies demonstrated that these powders with a tailored morphology exhibited increased deformability, resulting in improved deposition efficiency without compromising the mechanical properties of the coated layer. Liquid metal dealloying, applicable to various metals and featuring numerous controllable parameters, emerges as a versatile technique to produce such powders with a controlled structure.

CRediT authorship contribution statement

Louis Lesage: Writing – original draft, Visualization, Methodology, Investigation, Formal analysis, Conceptualization. **Christophe Le Bourlot:** Validation, Methodology, Data curation. **Eric Maire:** Writing – review & editing, Supervision, Investigation, Conceptualization. **Takeshi Wada:** Writing – review & editing, Supervision. **Hidemi Kato:** Writing – review & editing, Supervision. **Wolfgang Ludwig:** Investigation. **Nicolas Mary:** Writing – review & editing, Supervision, Project administration, Methodology, Funding acquisition, Conceptualization. **Pierre-Antoine Geslin:** Writing – review & editing, Supervision, Project administration, Investigation, Funding acquisition, Formal analysis, Conceptualization.

Declaration of competing interest

The authors declare that they have no known competing financial interests or personal relationships that could have appeared to influence the work reported in this paper.

Acknowledgements

We acknowledge the European Synchrotron Radiation Facility (ESRF) for the provision of synchrotron beamtime under the proposal MA5614. We would like to thank Pierre-Olivier Autran and Pedro Damas-Resende for their assistance and support in using beamline ID11. We are also grateful to Benjamin Leflon, Gustavo Pinzon-Forero and William Goncalves for their help during the experiment. We acknowledge the support of the EPOPEE project by LABEX MANUTECH-SISE (ANR-10-LABX-0075) at Université de Lyon, within the framework of the Plan France 2030 operated by the French National Research Agency (ANR). Finally, we acknowledge Dr. Peisheng Wang for providing his thermodynamic database file for the FeNiMg system. This work was performed within the framework of the International Research Network ELyT Global.

References

[1] Y. Ding, M. Chen, Nanoporous metals for catalytic and optical applications, MRS Bull. 34 (8) (2009) 569–576.
[2] R. Song, J. Han, M. Okugawa, R. Belosludov, T. Wada, J. Jiang, D. Wei, A. Kudo, Y. Tian, M. Chen, et al., Ultrafine nanoporous intermetallic catalysts by high-temperature liquid metal dealloying for electrochemical hydrogen production, Nature Commun. 13 (1) (2022) 5157.
[3] T. Wada, T. Ichitsubo, K. Yubuta, H. Segawa, H. Yoshida, H. Kato, Bulk-nanoporous-silicon negative electrode with extremely high cyclability for lithium-ion batteries prepared using a top-down process, Nano Lett. 14 (8) (2014) 4505–4510.
[4] T. Wada, J. Yamada, H. Kato, Preparation of three-dimensional nanoporous si using dealloying by metallic melt and application as a lithium-ion rechargeable battery negative electrode, J. Power Sources 306 (2016) 8–16.
[5] T. Wada, K. Yubuta, A. Inoue, H. Kato, Dealloying by metallic melt, Mater. Lett. 65 (7) (2011) 1076–1078.
[6] I. McCue, A. Karma, J. Erlebacher, Pattern formation during electrochemical and liquid metal dealloying, MRS Bull. 43 (1) (2018) 27–34.
[7] X. Guo, C. Zhang, Q. Tian, D. Yu, Liquid metals dealloying as a general approach for the selective extraction of metals and the fabrication of nanoporous metals: A review, Mater. Today Commun. 26 (2021) 102007.
[8] H.W. Pickering, Characteristic features of alloy polarization curves, Corros. Sci. 23 (10) (1983) 1107–1120.
[9] J. Erlebacher, M.J. Aziz, A. Karma, N. Dimitrov, K. Sieradzki, Evolution of nanoporosity in dealloying, Nature 410 (6827) (2001) 450–453.
[10] Y. Sun, Y. Ren, New preparation method of porous copper powder through vacuum dealloying, Vacuum 122 (2015) 215–217.
[11] X. Liu, A. Ronne, L.-C. Yu, Y. Liu, M. Ge, C.-H. Lin, B. Layne, P. Halstenberg, D.S. Maltsev, A.S. Ivanov, et al., Formation of three-dimensional bicontinuous structures via molten salt dealloying studied in real-time by in situ synchrotron x-ray nano-tomography, Nature Commun. 12 (1) (2021) 3441.
[12] J.W. Kim, M. Tsuda, T. Wada, K. Yubuta, S.G. Kim, H. Kato, Optimizing niobium dealloying with metallic melt to fabricate porous structure for electrolytic capacitors, Acta Mater. 84 (2015) 497–505.
[13] M. Mokhtari, C. Le Bourlot, J. Adrien, S. Dancette, T. Wada, J. Duchet-Rumeau, H. Kato, E. Maire, Cold-rolling influence on microstructure and mechanical properties of NiCr-Ag composites and porous nicr obtained by liquid metal dealloying, J. Alloys Compd. 707 (2017) 251–256.
[14] T. Wada, P.-A. Geslin, D. Wei, H. Kato, Partial liquid metal dealloying to synthesize nickel-containing porous and composite ferrous and high-entropy alloys, Commun. Mater. 4 (1) (2023) 43.
[15] T. Wada, P.-A. Geslin, H. Kato, Preparation of hierarchical porous metals by two-step liquid metal dealloying, Scr. Mater. 142 (2018) 101–105.
[16] P.-A. Geslin, I. McCue, B. Gaskey, J. Erlebacher, A. Karma, Topology-generating interfacial pattern formation during liquid metal dealloying, Nature Commun. 6 (1) (2015) 8887.
[17] I. McCue, B. Gaskey, P.-A. Geslin, A. Karma, J. Erlebacher, Kinetics and morphological evolution of liquid metal dealloying, Acta Mater. 115 (2016) 10–23.
[18] L. Lesage, T. Suga, T. Wada, H. Kato, C. Le Bourlot, E. Maire, N. Mary, P.-A. Geslin, A diffusion model for liquid metal dealloying. Application to NiCu precursors dealloyed in liquid ag, Acta Mater. 272 (2024) 119908.
[19] L. Lai, P.-A. Geslin, A. Karma, Microstructural pattern formation during liquid metal dealloying: Phase-field simulations and theoretical analyses, Phys. Rev. Mater. 6 (9) (2022) 093803.
[20] A. Chuang, J. Baris, C. Ott, I. McCue, J. Erlebacher, A powder metallurgy approach to liquid metal dealloying with applications in additive manufacturing, Acta Mater. 238 (2022) 118213.
[21] L. Lai, B. Gaskey, A. Chuang, J. Erlebacher, A. Karma, Topological control of liquid-metal-dealloyed structures, Nature Commun. 13 (1) (2022) 2918.

[22] A. Chuang, J. Erlebacher, Challenges and opportunities for integrating dealloying methods into additive manufacturing, Materials 13 (17) (2020) 3706.
[23] P. Wang, J. Zhao, Y. Du, H. Xu, T. Gang, J. Fen, L. Zhang, C. He, S. Liu, H. Ouyang, Experimental investigation and thermodynamic calculation of the Fe–Mg–Mn and Fe–Mg–Ni systems, Int. J. Mater. Res. 102 (1) (2011) 6–16.
[24] A. Okulov, A. Volegov, J. Weissmüller, J. Markmann, I. Okulov, Dealloying-based metal-polymer composites for biomedical applications, Scr. Mater. 146 (2018) 290–294.
[25] M. Mokhtari, C. Le Bourlot, J. Adrien, A. Bonnin, W. Ludwig, P.-A. Geslin, T. Wada, J. Duchet-Rumeau, H. Kato, E. Maire, In situ observation of liquid metal dealloying and etching of porous FeCr by X-ray tomography and X-ray diffraction, Materialia 18 (2021) 101125.
[26] Y.-C.K. Chen-Wiegart, S. Wang, W.-K. Lee, I. McNulty, P.W. Voorhees, D.C. Dunand, In situ imaging of dealloying during nanoporous gold formation by transmission x-ray microscopy, Acta Mater. 61 (4) (2013) 1118–1125.
[27] Y.-C.K. Chen-Wiegart, S. Wang, I. McNulty, D.C. Dunand, Effect of Ag–Au composition and acid concentration on dealloying front velocity and cracking during nanoporous gold formation, Acta Mater. 61 (15) (2013) 5561–5570.
[28] J.-O. Andersson, T. Helander, L. Höglund, P. Shi, B. Sundman, Thermo-calc & dictra, computational tools for materials science, CALPHAD 26 (2) (2002) 273–312.
[29] Thermo-calc software TCFE10 steels/fe-alloys database, 2024, https://thermocalc.com/products/databases/steel-and-fe-alloys/. (Accessed 6 February 2024).
[30] T. Wada, H. Kato, Three-dimensional open-cell macroporous iron, chromium and ferritic stainless steel, Scr. Mater. 68 (9) (2013) 723–726.
[31] Y.B. Jeong, T. Wada, S.-H. Joo, J.-M. Park, H.S. Kim, I.V. Okulov, K.B. Kim, H. Kato, Hierarchical heterostructured FeCr–(Mg–Mg2Ni) composite with 3D interconnected and lamellar structures synthesized by liquid metal dealloying, J. Mater. Res. Technol. 15 (2021) 4573–4579.
[32] M. Mokhtari, C. Le Bourlot, J. Adrien, A. Bonnin, T. Wada, J. Duchet-Rumeau, H. Kato, E. Maire, Microstructure characterization by X-ray tomography and EBSD of porous FeCr produced by liquid metal dealloying, Mater. Charact. 144 (2018) 166–172.
[33] L. Lutterotti, et al., Maud: a Rietveld analysis program designed for the internet and experiment integration, Acta Crystallogr. A 56 (s1) (2000) 54.
[34] H.M. Rietveld, A profile refinement method for nuclear and magnetic structures, J. Appl. Crystallogr. 2 (2) (1969) 65–71.
[35] R. Young, E. Prince, R. Sparks, Suggested guidelines for the publication of rietveld analyses and pattern decomposition studies, J. Appl. Crystallogr. 15 (3) (1982) 357–359.
[36] D. Chateigner, Combined Analysis, John Wiley & Sons, 2013.
[37] C.A. Schneider, W.S. Rasband, K.W. Eliceiri, NIH Image to ImageJ: 25 years of image analysis, Nat. Methods 9 (7) (2012) 671–675.
[38] C.L. Tsao, S.W. Chen, Interfacial reactions in the liquid diffusion couples of Mg/Ni, Al/Ni and Al/(Ni)-Al 2 o 3 systems, J. Mater. Sci. 30 (1995) 5215–5222.
[39] M. Tsai, M. Chou, C. Kao, Interfacial reaction and the dominant diffusing species in Mg–Ni system, J. Alloys Compd. 471 (1–2) (2009) 90–92.
[40] M. Tsuda, T. Wada, H. Kato, Kinetics of formation and coarsening of nanoporous α-titanium dealloyed with Mg melt, J. Appl. Phys. 114 (11) (2013).
[41] S.-H. Joo, T. Wada, H. Kato, Development of porous FeCo by liquid metal dealloying: Evolution of porous morphology and effect of interaction between ligaments and melt, Mater. Des. 180 (2019) 107908.
[42] T. Iida, Physical properties of liquid metals [IV] surface tension and electronic transport properties of liquid metals, Weld. Int. 8 (10) (1994) 766–770.
[43] L. Kaufman, M. Cohen, The martensitic transformation in the iron-nickel system, JOM 8 (1956) 1393–1401.
[44] K. Reuter, D.B. Williams, J. Goldstein, Determination of the Fe-Ni phase diagram below 400 C, Metall. Trans. A 20 (1989) 719–725.
[45] P.-A. Geslin, M. Buchet, T. Wada, H. Kato, Phase-field investigation of the coarsening of porous structures by surface diffusion, Phys. Rev. Mater. 3 (8) (2019) 083401.
[46] M. Hayase, M. Shiga, Y. Nakamura, Spontaneous volume magnetostriction and lattice constant of face-centered cubic Fe-Ni and Ni-Cu alloys, J. Phys. Soc. Japan 34 (4) (1973) 925–933.
[47] L. Swartzendruber, V. Itkin, C. Alcock, The Fe-Ni (iron-nickel) system, J. Phase Equilib. 12 (1991) 288–312.
[48] A. Volegov, S. Andreev, N. Selezneva, I. Ryzhikhin, N. Kudrevatykh, L. Mädler, I. Okulov, Additive manufacturing of heavy rare earth free high-coercivity permanent magnets, Acta Mater. 188 (2020) 733–739.
[49] T. Wada, K. Yubuta, H. Kato, Evolution of a bicontinuous nanostructure via a solid-state interfacial dealloying reaction, Scr. Mater. 118 (2016) 33–36.
[50] K. Kurabayashi, T. Wada, H. Kato, Dissimilar joining of immiscible Fe–Mg using solid metal dealloying, Scr. Mater. 230 (2023) 115404.
[51] B. Gaskey, I. McCue, A. Chuang, J. Erlebacher, Self-assembled porous metal-intermetallic nanocomposites via liquid metal dealloying, Acta Mater. 164 (2019) 293–300.
[52] H. Assadi, H. Kreye, F. Gärtner, T. Klassen, Cold spraying–a materials perspective, Acta Mater. 116 (2016) 382–407.
[53] P.-H. Gao, Y.-G. Li, C.-J. Li, G.-J. Yang, C.-X. Li, Influence of powder porous structure on the deposition behavior of cold-sprayed WC-12Co coatings, J. Therm. Spray Technol. 17 (2008) 742–749.
[54] J. Tang, Z. Zhao, N. Li, X. Qiu, Y. Shen, X. Cui, H. Du, J. Wang, T. Xiong, Influence of feedstock powder on microstructure and mechanical properties of Ta cold spray depositions, Surf. Coat. Technol. 377 (2019) 124903.
[55] X.-T. Luo, C.-X. Li, F.-L. Shang, G.-J. Yang, Y.-Y. Wang, C.-J. Li, WC-Co composite coating deposited by cold spraying of a core–shell-structured WC-Co powder, J. Therm. Spray Technol. 24 (2015) 100–107.
[56] L. He, D. Veysset, I.M. Nault, V.K. Champagne, M. Hassani, Impact and bonding behavior of core–shell powder particles, Surf. Coat. Technol. 441 (2022) 128591.